https://doi.org/10.5194/egusphere-2026-1581
Preprint. Discussion started: 17 April 2026

The Effect of Seawater Spatial density heterogeneity on Storm Surges — A Case Study of Typhoon "In-Fa" and Hangzhou Bay and Its Adjacent Waters

Yang Cuizhu[1, 2], Zhou Feng*[2, 1, 3]

1. School of Oceanography, Shanghai Jiao Tong University, Shanghai 200030, China
2. State Key Laboratory of Satellite Ocean Environment Dynamics, Second Institute of Oceanography, Ministry of Natural Resources, Hangzhou, Zhejiang 310012, China
3. Field Observation and Research Station of Yangtze River Delta Marine Ecosystem, Ministry of Natural Resources, Zhoushan, Zhejiang 316021, China

First Author of the Paper, Email: yangcuizhu@iscas.ac.cn

* Corresponding author, Email: zhoufeng@sio.org.cn

Abstract: Previous studies have shown that considering spatial density heterogeneity can improve the simulation capability and accuracy of water level, including storm surges, but the underlying dynamical mechanisms remain unclear. In this study, we conducted two contrasting models by FVCOM— a heterogeneous ocean model and a homogeneous ocean model to simulate water levels in Hangzhou Bay during the passage of Typhoon In-Fa in July 2021. We analyzed the spatiotemporal distribution characteristics of storm surges, and investigated carefully the mechanisms of storm surges by which spatial density heterogeneity. The simulation results show that both models perform comparably and with high accuracy in simulating astronomical tides and storm surges outside Hangzhou Bay. However, there are significant differences emerge in simulating storm surges inside Hangzhou Bay, where the heterogeneous ocean model substantially outperforms the homogeneous ocean model, with a maximum error of less than 0.2 m compared to 0.9 m for the latter, approximately 25% of the maximum storm surge. Based on the magnitude and duration of storm surge rise and fall, the interior and exterior of Hangzhou Bay exhibit two distinctly different situations: the interior is characterized by large surge amplitudes with durations exceeding 2 days, while the exterior shows smaller amplitudes with durations of approximately half a day. Dynamical analysis reveals that in regions where the storm surge duration exceeds the inertial period (e.g., the interior of Hangzhou Bay), the part of the storm surge affected by density can be expressed as a coupled form of the product of the density Laplacian and a quadratic term of the storm surge. In regions where the density Laplacian is negative (i.e., the density surface is convex upward), the part of the storm surge affected by density is negative during the surge rise phase, thereby reducing the overestimation bias of the homogeneous model; during the surge fall phase, it becomes positive, reducing the underestimation bias. In regions where

https://doi.org/10.5194/egusphere-2026-1581
Preprint. Discussion started: 17 April 2026

the density Laplacian is positive, the above effects are reversed.

Keywords: storm surge; spatial density heterogeneity; density–storm surge coupling

https://doi.org/10.5194/egusphere-2026-1581
Preprint. Discussion started: 17 April 2026

1 Introduction

Storm surges are one of the most destructive marine hazards, which can contribute to more than 95% of the total economic losses caused by marine disasters in coastal areas (China Marine Disaster Bulletin, Ministry of Natural Resources, 2024). It is important for people to understand the mechanisms of storm surges and then make accurate forecasts. Before the 1970s, many studies focused on the shallow water equation theory (Doodson, 1956; Heaps, 1969) to explain the phenomenon of storm surges. From the 1980s to present, benefiting from the progress of technology, more and more in-depth investigations of storm surges have been conducted through numerical model simulations. These studies pay more attention to the main effects of typhoons, astronomical tides, and wind waves on storm surge forecast accuracy, and have gotten many detailed conclusions (Yu et al., 2020). However, few studies consider the spatial density heterogeneity's effects on storm surges. In recent years, there are some studies which have observed that spatial density heterogeneity can significantly affect storm surge forecast accuracy. Among them, there are three dynamical mechanisms are considered to account for: coastal trapped waves, bottom friction, and pressure gradient force. Each factor can affect storm surges in different ways, but need more in-depth investigation.

Certain coastal trapped waves may exert an influence on storm surges within regions characterized by strong water density stratification, such as certain low-latitude coastal zones and adjacent shelf margins. In weakly stratified, wide-shelf, high-latitude waters, where Bu << 1, coastal trapped waves approximate barotropic shelf waves; conversely, in strongly stratified, narrow-shelf, near-equatorial waters, where Bu >> 1, coastal trapped waves more closely resemble internal Kelvin waves. Some relevant studies have observed that storm surges are also affected in regions where coastal trapped waves propagate prominently. Kodaira et al. (2016) made a comparative study using barotropic and baroclinic models to investigate storm surges at 257 tide gauge stations worldwide in 2014. The results showed that the baroclinic model improved storm surge forecast accuracy at nearly all stations, but the degree of improvement varied. The greatest improvement was found near the East

https://doi.org/10.5194/egusphere-2026-1581
Preprint. Discussion started: 17 April 2026

London station on the southeastern coast of Africa, reaching about 10 cm, other stations' improvements are in the range of 3 cm to 4 cm. The authors pointed out that it may be the topography change the storm surge forecast accuracy in the baroclinic model. In the area where the continental shelf rapidly narrows in southern Africa, the amplitude of coastal trapped waves increases significantly, leading to a significant change in storm surge forecast accuracy. Wang et al. (2022) made a comparative study using barotropic and baroclinic models to examine total water levels, astronomical tides, and residual water levels at 211 global tide gauge stations from 2019 to 2021 across multiple timescales (seasonal, inter-seasonal, sub-seasonal, and weather-scale). The results showed that the baroclinic model improved simulation accuracy for all stations relative to the barotropic model. In the eastern Indian Ocean, where the greatest improvement in extreme residual water levels at the weather timescale has been found, reaching up to 42 cm. In the area, the authors also attributed the changes of storm surges to coastal trapped waves. Scale analysis pointed out that the Burger number in this region is much greater than 1, and the associated waves have a longer critical period affected by the slanted coastline— both factors favor the formation of coastal trapped waves in the baroclinic model, and then the storm surge is also influenced.

Bottom friction is also considered to alter the storm surge forecast accuracy due to the density stratification. In the study by Kodaira et al. (2016), an notable improvement in storm surge forecast accuracy was found at the Naha station in Japan, which was directly in the path of the typhoon. The comparative experiments showed that the storm surge height in the baroclinic model was greater than that in the barotropic model, and the authors suggested that the bottom friction affected the accuracy of storm surge, but there was no clear evidence. Orton et al. (2012) made sensitivity numerical experiments to simulate two storm surge events in the Hudson River estuary and analyzed five physical processes influencing storm surges. The results took an order of the extent of precision variation resulting from the above physical processes, and the effect of density variation was second and the atmospheric forcing was first. The result showed that the storm surge forecast accuracy improved by 1%–5% in the lower river and offshore areas, and up to 13% in the upper river. The authors thought that the stratified water column and the weakened turbulent mixing caused the accuracy change. This finding is similar to the work of Muller, who researched the mechanisms

https://doi.org/10.5194/egusphere-2026-1581
Preprint. Discussion started: 17 April 2026

underlying seasonal variations in tidal amplitude on shallow continental shelves. Through analytical solutions and numerical modeling, Muller concluded that stratification of water column can modify the eddy viscosity profile and bottom friction, thereby affecting tidal transport and causing changes in tidal amplitude.

The pressure gradient force caused by spatial density heterogeneity is also an important factor affecting storm surge forecast accuracy. Ye et al. (2020) made a comparative study using barotropic and baroclinic models to study storm surges during a typhoon event. The results showed that the baroclinic model had higher accuracy. Besides, the difference in water levels between the two models was relatively small during the storm surge rising, but became obviously larger during the storm surge falling. The baroclinic model reduced the error of the barotropic model by 14%. The authors thought that the large-scale baroclinic effect of the Gulf Stream may reduce the error. Pringle et al. (2019) made a comparative experiment using barotropic and baroclinic models to research the influence of the density on storm surges around Puerto Rico and the U.S. Virgin Islands. The results showed that the baroclinic model had the smallest errors. At most tide gauge stations, storm surge peaks in the baroclinic model were 10–20 cm taller than the barotropic model, what's more, water levels in the baroclinic model were 10–15 cm lower than the levels before the typhoon. The authors thought that this water level depression may be related to the pressure gradient force because of deep-water upwelling in that region.

In summary, spatial density heterogeneity can obviously affect the capability and accuracy of numerical models in simulating storm surges. However, the reasons why there were the accuracy change were unclear. The above studies just gave the conjecture, such as coastal trapped waves, the bottom friction, and large-scale ocean circulation, which need more rigorous analysis. According to this research background, the present study takes Typhoon In-Fa as a case study and selects Hangzhou Bay as the study area, to investigate the dynamical mechanisms by which spatial density heterogeneity affects storm surges.

2 Data and Methods

https://doi.org/10.5194/egusphere-2026-1581
Preprint. Discussion started: 17 April 2026

The study area is Hangzhou Bay, as shown in Fig. 1. This region is affected by typhoons frequently (Hou et al., 2011). In 2021, strong Typhoon In-Fa made landfall in Zhoushan and subsequently traversed Hangzhou Bay, exerting an important impact on the region. Fig. 1a shows the track and intensity variation of Typhoon In-Fa; Fig. 1b shows the specific spatial location and current field characteristics of the study area. The region is situated in northern Zhejiang Province on the southern flank of the Yangtze River Delta, Zhoushan Archipelago is to the east. The mouth of the bay is defined by the line connecting Lu chao gang (A) to Zhen hai (B), the width is approximately 98 km, a mean water depth of approximately 10 m. The density field in this region is jointly influenced by the Yangtze River diluted water, the Taiwan Warm Current, and the Zhe-Min Coastal Current, different currents have different density, resulting in obvious spatial density heterogeneity. This makes the region an ideal study area for researching the influence of spatial density heterogeneity on storm surges.

There are two kinds of data, one is the observed data and the other is the simulated data. The observed data contains typhoon data and water level records from tide gauge stations. In addition, two storm surge simulation experiments are using the FVCOM forced by Typhoon In-Fa: a homogeneous ocean model (HM), in which seawater density keeps a constant value, and a heterogeneous ocean model (HT), in which density varies spatially. In the two experiments, only the density condition is different, and all other conditions remain unchanged.

https://doi.org/10.5194/egusphere-2026-1581
Preprint. Discussion started: 17 April 2026

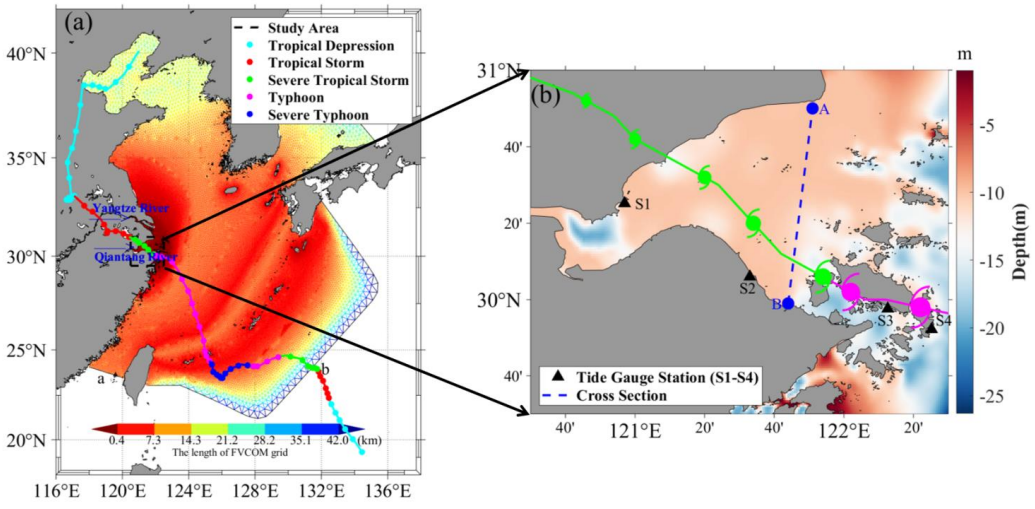

Fig. 1a Model grid resolution and the track of Typhoon In-Fa; Fig. 1b water depth (color shading), tide gauge stations, track of Typhoon In-Fa, and transects.

2.1 Overview of Typhoon In-Fa

Information on the 2021 No. 6 strong Typhoon In-Fa was obtained from the China Typhoon Meteorological Network (http://typhoon.nmc.cn), including the track, maximum wind speed, translation speed, translation direction, and radius of maximum wind. The track and intensity of Typhoon In-Fa at different stages are shown in Fig. 1a. Tropical Storm In-Fa formed over the northwestern Pacific Ocean on July 16, 2021, and then developed into a tropical storm on July 18. At approximately 12:30 on July 25, it made landfall in Putuo District, Zhoushan City, the level of intensity is typhoon, which had a maximum wind speed of 38 m/s, traversed Hangzhou Bay along the northwestward direction. By 03:00 on July 28, it had weakened to a tropical depression with a wind speed of 15 m/s. During its passage through Hangzhou Bay,Typhoon In-Fa had a significant impact on water levels. Based on the basic parameters of Typhoon In-Fa, the typhoon wind field was produced by the method proposed by Emanuel (2004), in which the wind speed at the radius of maximum wind is given by the following formula:

https://doi.org/10.5194/egusphere-2026-1581
Preprint. Discussion started: 17 April 2026

$$U(r)=\frac{R_m(2CU_m-U_t\sin(\theta))r+\frac{1}{2}R_m^2 fr}{R_m^2+r^2}-\frac{fr}{2} \quad (1)$$

Where $C=0.736$ is the correction coefficient for the maximum wind speed U_m, U_t is the translation speed, R_m is the radius of maximum wind, θ is the translation direction, and f is the Coriolis parameter (Xuan et al., 2021).

2.2 Observed Water Level Data

In accordance with the track of Typhoon In-Fa through Hangzhou Bay, four tide gauge stations were selected for water level records: Ganpu (S1), Gaobeipu (S2), Changzhi (S3), and Shenjiamen (S4). Hourly water level records are used in this study. S1 is located in the innermost part of Hangzhou Bay, S2 is in the central portion of the bay, and S3 and S4 are located outside the bay. The four stations collectively provide a representative picture of water level variations in different sub-regions during the passage of Typhoon In-Fa. Detailed information on the water level data is provided in Section 3.1.

2.3 Numerical Model Description

We use the Finite Volume Community Ocean Model (FVCOM) to simulate storm surges. FVCOM employs the unstructured triangular grids that can flexibly adapt to complex coastline geometries, strengthen the resolution in coastal regions, and also accommodate shallow water environments such as estuaries and nearshore areas.

We take the HT model as an example to illustrate the characteristics of the model configuration. First, the water depth in the vertical direction is interpolated from the bathymetric data of the General Bathymetric Chart of the Oceans (GEBCO). A sigma coordinate system uniformly divided into 20 layers is adopted in the vertical direction. In the horizontal direction, spherical coordinates are used, and the Surface-water Modeling System (SMS) are using to generate a high-resolution unstructured triangular grid. The horizontal grid resolution is approximately 1 km in the Yangtze River Estuary region and decreases to approximately 9 km in areas farther away. The model has three open

https://doi.org/10.5194/egusphere-2026-1581
Preprint. Discussion started: 17 April 2026

boundaries: the Taiwan Strait to the southwest (a), the northwestern Pacific Ocean to the southwest, south, and southeast (b), and the Japan Sea to the north (c) (not shown in the figure).

The HT model is used again as an example to describe the model forcing, open boundary conditions, and initial field settings. The forcing in HT includes tidal currents, river discharge, heat flux, and wind field. The open boundary conditions include tidal elevation and mean flow. The initial fields of temperature, salinity, and mean flow are interpolated from the HYCOM data assimilation product (https://www.hycom.org/). Tidal currents are driven by tidal elevation at the open boundaries, which are obtained from Oregon State University Tidal Prediction Software (OTPS; http://volkov.oce.orst.edu/tides) global tidal model. Egbert et al. (1994) and Egbert and Erofeeva (2002) calculated the amplitudes and phase of 11 single tides: M_2, S_2, N_2, K_2, K_1, O_1, P_1, Q_1, M_4, MS_4, and MN_4. River discharge primarily considers the Yangtze River and Qiantang River, with Yangtze River discharge obtained from the Yangtze River Hydrology Network (www.cjh.com.cn) and Qiantang River discharge from the Ministry of Water Resources (http://www.mwr.gov.cn/sj/tjgb/zghlnsgb/). The daily mean heat flux is from the objectively analyzed air-sea fluxes (OAFlux; Yu and Weller, 2007). The wind field consists of two parts data, one is the ERA-Interim reanalysis data, the online address is https://www.ecmwf.int/en/forecasts/dataset/ecmwf-reanalysis-interim), and the other is the typhoon wind field in Equation (1).

The grid configuration of HM is the same as that of HT. In the HM, temperature and salinity are set to constant values of 20°C and 30 PSU, with all other settings remaining the same. Both models simulate water levels, temperature fields, salinity fields, and current fields from May 1 to July 31, 2021, and the output data is given every half hour.

3 Results

3.1 Comparison of Water Level Simulation Results between HM and HT

Based on the above configurations and the governing dynamical equations of FVCOM, we can get the water levels during the typhoon period. Since we take tidal currents as an important open

https://doi.org/10.5194/egusphere-2026-1581
Preprint. Discussion started: 17 April 2026

boundary condition, the simulated water levels were the total water levels, which contains astronomical tides. We use the t_tide toolbox to extract the storm surge signal. Complex processes such as tide–surge interaction are not considered in this study.

Firstly, we compare the total water levels in the two simulated models. The results are shown in Fig. 2. The root mean square error (RMSE) and correlation coefficient (CC) are chosen to evaluate the simulation capability of the two models. RMSE measures the magnitude of the deviation between simulated and observed values, CC measures the degree of correlation between simulated and observed values, the two values are used to assess simulation accuracy. In Fig. 2, the mean RMSE across the four stations is 0.08 m for HT and 0.22 m for HM, meaning that HM has considerably larger deviations from observed water levels .The mean CC across four stations is 0.998 for HT and 0.995 for HM; both values are relatively high, very similar to the observed water level, but HT remains slightly superior. Overall, HT demonstrates stronger capability and higher accuracy than HM in simulating total water levels.

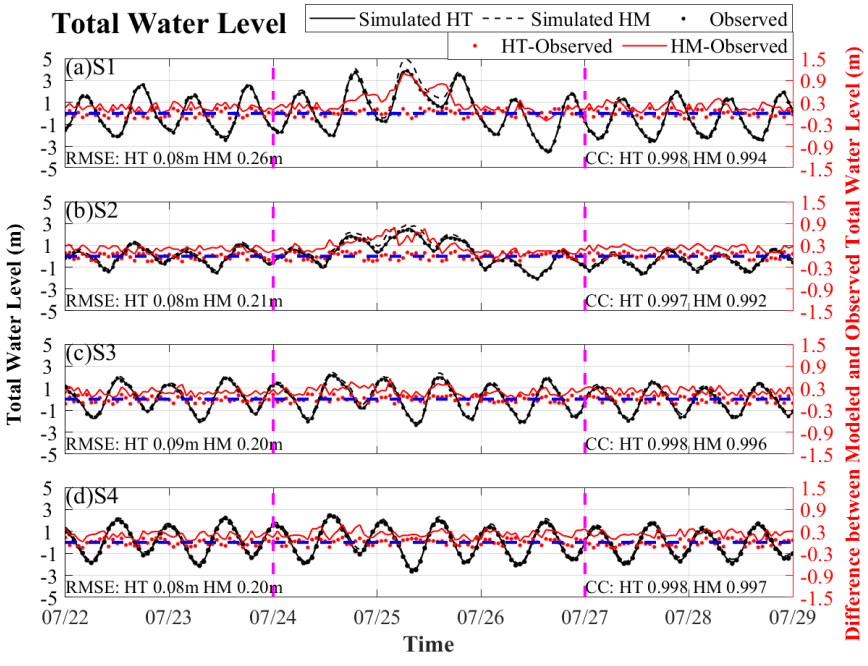

https://doi.org/10.5194/egusphere-2026-1581
Preprint. Discussion started: 17 April 2026

Fig. 2 Comparison of simulated and observed total water levels.

According to the different stages of Typhoon In-Fa's passage through Hangzhou Bay, we also compared the differences in astronomical tides and storm surges between the two models. Before July 24 and after July 27 are the periods for describing the astronomical tide . As shown in Fig. 2, before and after the typhoon, the astronomical tides are dominated by semi-diurnal tides with an amplitude of approximately 2 m. The deviation between HT model and the observed values is small, at approximately 0 m, whereas HM model displays considerably larger deviations, at approximately 0.25 m. The accuracy of astronomical tides in HT is improved by approximately 12.5% relative to HM.

After eliminating the astronomical tide from the total water level, the storm surges are shown in Fig. 3. There are different characteristics of surges. We divided them into two parts, one at S1-S2 and the other at S3-S4. At stations S1–S2, the surge rises up to nearly 4 m, after the peak, water levels decrease rapidly, and a storm surge depression is observed during the residual period, the level is approximately -2m. The overall duration of the surge rise and fall lasts 2–3 days. The deviation between HT-simulated and observed storm surges is small, whereas the deviation between HT-simulated and observed storm surges is larger, with the maximum discrepancy approaching 1.5 m. The storm surge forecast accuracy in HT is improved by approximately 38% relative to HM.

At stations S3–S4, the surge curves are of a mixed type, showing both oscillatory patterns and small-amplitude variations, with the values range from −0.6 m to 0.6 m, obviously smaller than those at S1–S2. The overall duration of the surge rise and fall is approximately 1–2 days. The deviation between HT-simulated and observed storm surges is small, while HM-simulated storm surges deviate considerably from the observations, with the discrepancy displaying a significant oscillatory pattern ranging from −0.2 m to 0.2 m. The storm surge forecast accuracy in HT is improved by approximately 30% relative to HM.

https://doi.org/10.5194/egusphere-2026-1581
Preprint. Discussion started: 17 April 2026

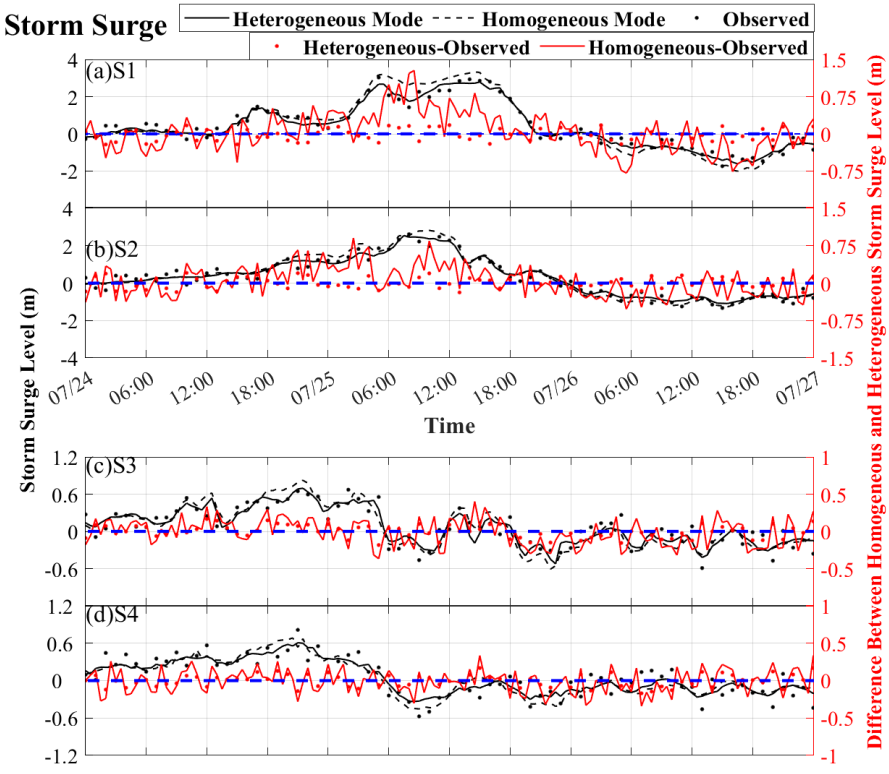

Fig. 3 Comparison of simulated and observed storm surges.

In summary, the HT model shows superior simulation capability and accuracy compared to the HM model for all water level types, including total water levels, astronomical tides, and storm surges. At different stations, for astronomical tides, the results are similar across all four stations, with the mean deviation of HM-simulated values are approximately 0.3 m; for storm surges ,there are obvious differences between stations S1–S2 and S3–S4: at S1–S2,the amplitudes are large during the rising time and falling time, and deviations of HM-simulated values from observations are correspondingly large, whereas at S3–S4, the amplitudes are small in the whole surging time, and the deviations of HM-simulated values from observations are also relatively small.

3.2 Spatiotemporal Distribution Characteristics of Storm Surges

https://doi.org/10.5194/egusphere-2026-1581
Preprint. Discussion started: 17 April 2026

Since HT models has more simulation accuracy, we choose the HT's results to represent the spatiotemporal variation characteristics of storm surges across the entire study area.

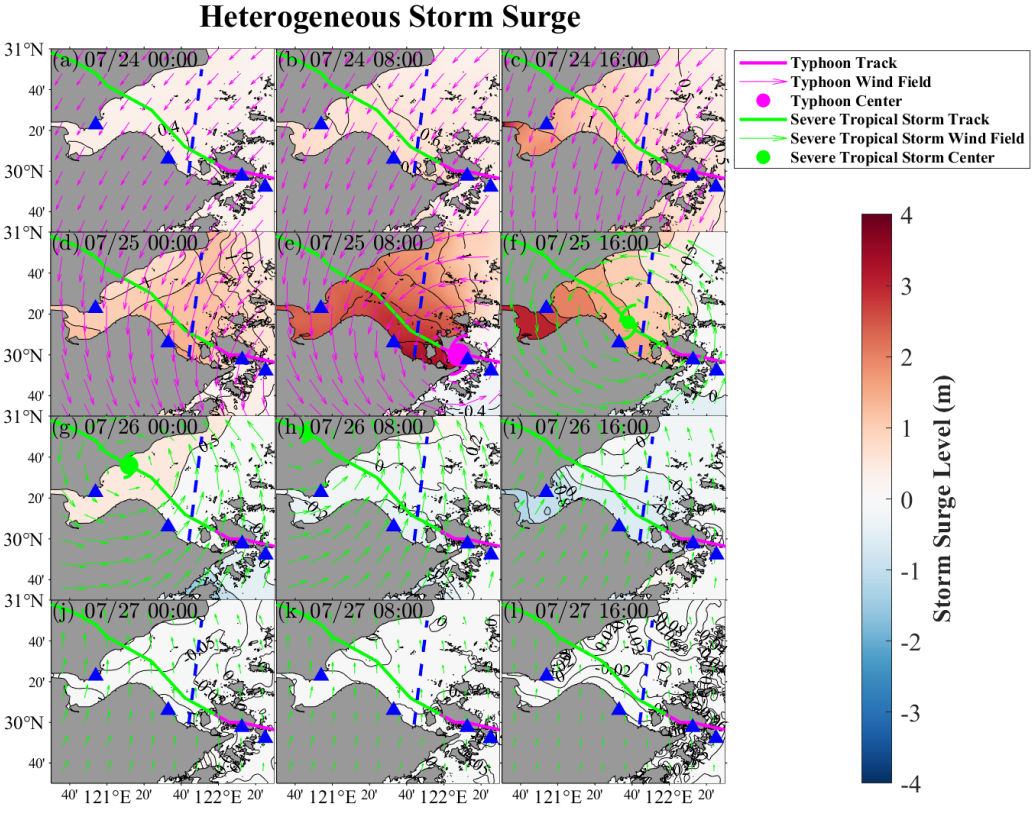

Fig. 4 Spatiotemporal variations of storm surges.

Fig. 4 shows the spatial distribution of storm surges per 8 hours from July 24 to July 27, including the initial surge rise, peak, and subsequent surge fall. The surge rise process unfolds as follows: a slight water level rise of less than 1 m appears across the entire study area at 08:00 on July 24; by 00:00 on July 25, the surge height increases with values exceed 1 m to the west of the bay mouth; by 08:00 on July 25, the surge reaches its maximum, with water levels inside Hangzhou Bay exceeding

https://doi.org/10.5194/egusphere-2026-1581
Preprint. Discussion started: 17 April 2026

3 m, while at 16:00 the elevated surge inside the bay is maintained while the surge outside decreases; by 00:00 on July 26, a notable water level drop is already evident; by 16:00 on July 26, a slight surge depression appears to the west of the bay mouth, with a maximum depression of −0.4 m inside Hangzhou Bay; by 00:00 on July 27, water levels have largely returned to normal. In terms of the spatial distribution of the surge, the bay and estuarine areas near stations S1 and S2 experience large surge rise and fall amplitudes, while the archipelago waters near stations S3 and S4 exhibit smaller surge rise with no surge depression observed.

In terms of typhoon intensity and track, the maximum surge occurs when the typhoon is at its greatest intensity and is located to the left of the typhoon track. For the typhoon's wind field, the primary surge rise period inside Hangzhou Bay corresponds to onshore winds from the northeast, while the primary surge fall period corresponds to offshore winds from the southwest. Overall, the spatial variations are governed by typhoon intensity, track, wind direction, and the topographic characteristics of different sub-regions.

According to the above results, the duration of the storm surge's rising and falling phases is approximately 2–3 days. So we take a wavelet analysis to determine the dominant periods of storm surges across the entire study area, as shown in Fig. 5.

https://doi.org/10.5194/egusphere-2026-1581
Preprint. Discussion started: 17 April 2026

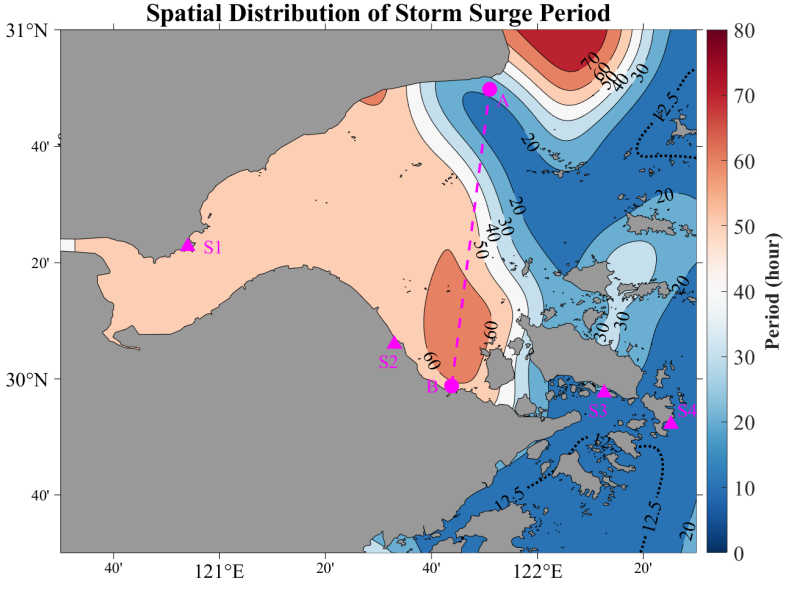

277

278 Fig. 5 Spatial distribution of storm surge periods across the study area.

279 Fig. 5 shows the spatial distribution of storm surge periods across the entire study area. There is
280 a bay mouth transect AB as the boundary, the dominant period inside Hangzhou Bay to the west is
281 50 h or above, while to the east it is 20 h or below, with the period increasing gradually from east to
282 west in the vicinity of the bay mouth. The inertial frequency across the study area is approximately
283 $7.3\times10^{-5}s^{-1}$, relative to which the storm surge frequency inside Hangzhou Bay is approximately
284 $3.5\times10^{-5}s^{-1}$, classifying it as a low-frequency storm surge, while the storm surge frequency outside
285 Hangzhou Bay is approximately $8.7\times10^{-5}s^{-1}$, classifying it as a high-frequency storm surge. Based
286 on the above results, storm surges around stations S1-S2 has a low-frequency, and the rising and
287 falling amplitudes are large and the differences between HM-simulated and observed storm surges
288 are also large. Storm surges around stations S3–S4 exhibit high-frequency characteristics, with small
289 rising and falling amplitudes and small differences between HM-simulated and observed storm surges.

https://doi.org/10.5194/egusphere-2026-1581
Preprint. Discussion started: 17 April 2026

3.3 Spatiotemporal Distribution Characteristics of Temperature, Salinity, and Density

Since observational data on temperature, salinity, and density in Hangzhou Bay and its adjacent waters during the passage of Typhoon In-Fa were not available, the physical quantities simulated by the heterogeneous ocean model (HT) are used to represent the real values. The model directly simulates the spatiotemporal distributions of temperature and salinity, while density is calculated using the Thermodynamic Equation of Seawater - 2010 (TEOS-10), which is the standard recommended by the international oceanographic community. In this process, the model-simulated temperature, given as potential temperature, and salinity, given as practical salinity, are first converted to conservative temperature and absolute salinity, respectively, before density is computed using the Gibbs function.

We first examine the spatiotemporal distribution characteristics of temperature, salinity, and density in the vertical direction at individual stations.

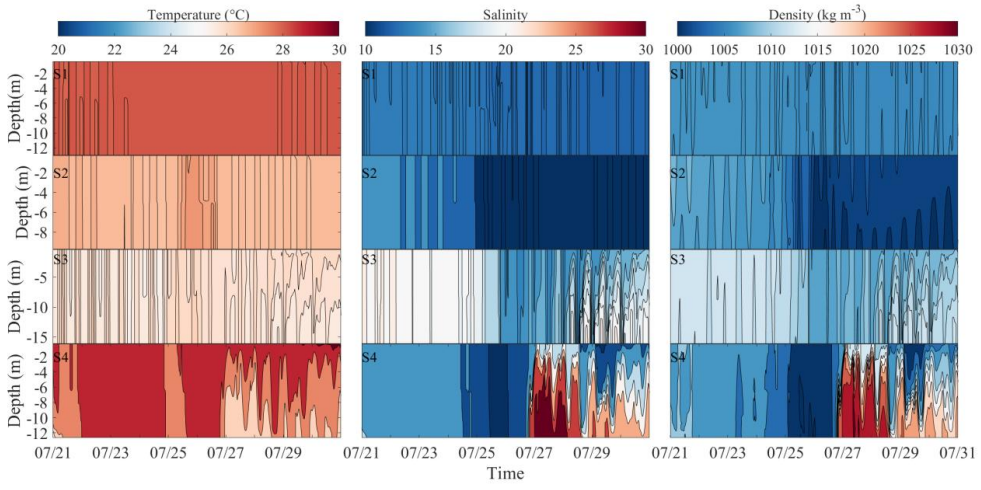

Fig. 6 Temporal evolution of vertical profiles of temperature, salinity, and density at stations S1–S4.

The density variations are similar to the salinity variations. The water depths at the four stations

https://doi.org/10.5194/egusphere-2026-1581
Preprint. Discussion started: 17 April 2026

are similar and small, with a mean depth of approximately 12 m. At stations S1–S2, temperature, salinity, and density are well mixed in the vertical direction. Specifically, there are no obvious changes at S1 and S2 before or after the typhoon. At stations S3–S4, the water column remains vertically well mixed before and during the typhoon, but the stratification develops during the surge falling period.

In general, at all four stations, temperature, salinity, and density are vertically well mixed both before and during the typhoon, so we use the depth-averaged values to represent the characteristics of the whole water column at each station. The following section presents the density variation characteristics of the entire study area when the typhoon passed through this area.

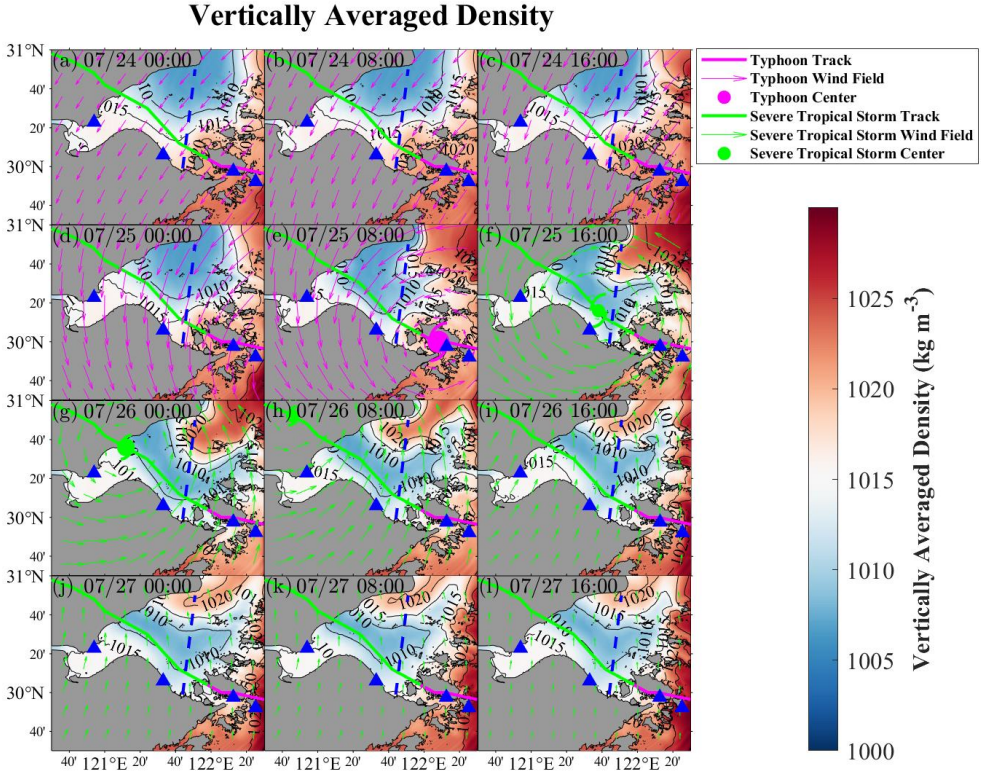

Fig. 7 Spatial distribution characteristics of depth-averaged density during the passage of the typhoon.

During the passage of the typhoon, the primary density changes occur outside Hangzhou Bay

https://doi.org/10.5194/egusphere-2026-1581
Preprint. Discussion started: 17 April 2026

and in the bay mouth region, while there is no notable density change in the interior or at the head of the bay. As the typhoon gradually moves northwestward, a high-density water tongue gradually develops in the bay mouth region and expands northwestward from 00:00 on July 24 to 00:00 on July 26, reaching its maximum areal extent at around 00:00 on July 26. After 00:00 on July 26, the areal extent of the water tongue gradually diminishes. Overall, the spatial distribution of density in this region displays a high–low–high pattern throughout the typhoon passage.

3.4 Analysis of the Mechanisms by Which Spatial density heterogeneity Influences Storm Surges

As demonstrated above, the HT model achieves significantly higher storm surge simulation accuracy than the HM model. To investigate the reasons for this improvement, the following analysis will use the govern equations about the water level and current field variations to progressively and clearly elucidate the mechanisms how the spatial density heterogeneity influences storm surges.

According to fundamental ocean dynamics theory, the spatiotemporal variations of water levels are essentially driven by the convergence and divergence of the current field. The continuity equation can precisely describe this progress. The current field itself is affected by all kinds of dynamical factors, including the Coriolis force, pressure gradient force, wind stress, surface wind force, bottom friction force, all of which can be comprehensively summarized by the momentum equation. On this basis, our goal is that to find the quantitative relationship between A and B by combing the continuity equation and momentum equations.

Because the change of the water level is associated with the whole column, the depth-integrated form of the equations in the vertical direction is required. Here the water level refers to the total water level variation at a given spatial point at a given time.

$$D(x,y,t) = H(x,y) + \eta(x,y,t) \tag{2}$$

Correspondingly, the depth-integrated velocity is defined as follows. Here, the velocity also refers to the total velocity at a given spatial point at a given time, which includes tidal currents as well as other flow components:

https://doi.org/10.5194/egusphere-2026-1581
Preprint. Discussion started: 17 April 2026

$$\vec{U} = \int_{-H}^{\eta} \vec{u}(x,y,z,t)\,dz \tag{3}$$

So, the continuity equation and momentum equation in vector form are given as follows:

$$\frac{\partial \eta}{\partial t} + \nabla \cdot \vec{U} = 0 \tag{4}$$

$$\frac{\partial \vec{U}}{\partial t} + \left(\frac{\vec{U}}{D} \cdot \nabla\right)\vec{U} + f\hat{k} \times \vec{U} = -gD\nabla\eta - \frac{g}{\rho_0}\left[\int_{-H}^{\eta} \nabla\left(\int_{z}^{\eta} \rho' dz'\right) dz\right] + \vec{\tau}_s - \vec{\tau}_b \tag{5}$$

To describe the individual terms in the momentum equation clearly, we use the following simplifications and notations. In the depth-integrated form, the advection term represents a nonlinear coupling between the vertically averaged velocity and the depth-integrated velocity. Here, the combined coupling term is treated as a nonlinear stress term:

$$\vec{N} = \left(\frac{\vec{U}}{D} \cdot \nabla\right)\vec{U} \tag{6}$$

in the homogeneous ocean model, the pressure gradient force caused by sea surface height variations is given as follows:

$$\vec{P} = gD\nabla\eta \tag{7}$$

in the heterogeneous ocean, the pressure gradient force caused by spatial density heterogeneity is given as follows:

$$\vec{P'} = \frac{g}{\rho_0}\left[\int_{-H}^{\eta} \nabla\left(\int_{z}^{\eta} \rho' dz'\right) dz\right] \tag{8}$$

the sea surface wind stress is given as follows:

$$\vec{\tau}_s = C_{ds}|U_w|\vec{U}_w \cdot \rho_{air}/\rho_0 \tag{9}$$

the bottom friction force is given as follows:

$$\vec{\tau}_b = C_{db}|U_b|\vec{U}_b \tag{10}$$

where $g = 9.8 m/s^2$ is the gravitational acceleration; U_w is the wind speed and U_b is the bottom layer current velocity; the wind stress coefficient C_{ds} is 0.0012 (Bernier and Thompson, 2015), the bottom friction coefficient is 0.0025 (Chen et al., 2003), $\rho_{air} = 1 kg/m^3$ is the air density, and the

https://doi.org/10.5194/egusphere-2026-1581
Preprint. Discussion started: 17 April 2026

seawater density in the wind stress calculation takes a reference value $\rho_0 = 1020 kg/m^3$. After undergoing these treatments, the simplified momentum equation is given as follows:

$$\frac{\partial \vec{U}}{\partial t} + f\hat{k} \times \vec{U} = -\vec{P} - \vec{P'} - \vec{N} + \vec{\tau}_s - \vec{\tau}_b \tag{11}$$

take the divergence of Equation (11):

$$\frac{\partial}{\partial t}\left(\nabla \cdot \vec{U}\right) - f\left(\nabla \times \vec{U}\right) = -\nabla \cdot \left(\vec{P} + \vec{P'} + \vec{N} - \vec{\tau}_s + \vec{\tau}_b\right) \tag{12}$$

taking the curl of Equation (11):

$$\frac{\partial}{\partial t}\left(\nabla \times \vec{U}\right) + f\left(\nabla \cdot \vec{U}\right) = -\nabla \times \left(\vec{P} + \vec{P'} + \vec{N} - \vec{\tau}_s + \vec{\tau}_b\right) \tag{13}$$

$\frac{\partial (12)}{\partial t} + f \times (13)$ eliminating the vorticity term: $\left(\nabla \times \vec{U}\right)$:

,

$$\frac{\partial^2}{\partial t^2}\left(\nabla \cdot \vec{U}\right) - f\frac{\partial\left(\nabla \times \vec{U}\right)}{\partial t} = -\frac{\partial\left[\nabla \cdot \left(\vec{P} + \vec{P'} + \vec{N} - \vec{\tau}_s + \vec{\tau}_b\right)\right]}{\partial t} \tag{14}$$

$$f^2\left(\nabla \cdot \vec{U}\right) + f\frac{\partial\left(\nabla \times \vec{U}\right)}{\partial t} = -f\left[\nabla \times \left(\vec{P} + \vec{P'} + \vec{N} - \vec{\tau}_s + \vec{\tau}_b\right)\right] \tag{15}$$

$$\frac{\partial^2}{\partial t^2}\left(\nabla \cdot \vec{U}\right) + f^2\left(\nabla \cdot \vec{U}\right) = -f\left[\nabla \times \left(\vec{P} + \vec{P'} + \vec{N} - \vec{\tau}_s + \vec{\tau}_b\right)\right] - \frac{\partial\left[\nabla \cdot \left(\vec{P} + \vec{P'} + \vec{N} - \vec{\tau}_s + \vec{\tau}_b\right)\right]}{\partial t} \tag{16}$$

eliminating the divergence term using the continuity equation: $\left(\nabla \cdot \vec{U}\right)$, the final equation governing water level variations is obtained as:

$$f^2\frac{\partial \eta}{\partial t} + \frac{\partial^3 \eta}{\partial t^3} = f\left[\nabla \times \left(\vec{P} + \vec{P'} + \vec{N} - \vec{\tau}_s + \vec{\tau}_b\right)\right] + \frac{\partial\left[\nabla \cdot \left(\vec{P} + \vec{P'} + \vec{N} - \vec{\tau}_s + \vec{\tau}_b\right)\right]}{\partial t} \tag{17}$$

Equation (17) is the governing dynamical equation describing the relationships between water level variations and various dynamical forcing factors. The left-hand side shows water level variations at different timescales, while the right-hand side shows several dynamical factors at different timescales in the form of vorticity and divergence. Since this study focuses on storm surge variations, and as described in Section 2.1, the storm surge is obtained by subtracting the harmonically predicted astronomical tide from the total water level at the corresponding time step. Accordingly, harmonic analysis is also applied to each term in Equation (17) in order to remove the influence of astronomical tides.

https://doi.org/10.5194/egusphere-2026-1581
Preprint. Discussion started: 17 April 2026

We firstly analyze the storm surge variations represented on the left-hand side of Equation (17). $f^2\frac{\partial\eta}{\partial t}$ represents the variation of storm surge influenced by the Earth's rotation effect, while $\frac{\partial^3\eta}{\partial t^3}$ represents the variation of storm surge governed by its own period. Based on the previous analysis, the dominant period of storm surges inside Hangzhou Bay exceeds 50 h, the storm surge variations are primarily dominated by $f^2\frac{\partial\eta}{\partial t}$.

We next analyze the right-hand side of Equation (17). Since this equation includes the pressure gradient force generated by spatial density heterogeneity, it effectively represents the dynamical equation under the HT model. To combine with HM model, Equation (17) is rewritten as follows:

$$\left(f^2\frac{\partial\eta}{\partial t}+\frac{\partial^3\eta}{\partial t^3}\right)_{HT}=\left\{f\left[\nabla\times\left(\vec{P}+\vec{N}-\vec{\tau}_s+\vec{\tau}_b\right)\right]+\frac{\partial\left[\nabla\cdot\left(\vec{P}+\vec{N}-\vec{\tau}_s+\vec{\tau}_b\right)\right]}{\partial t}\right\}_{HT}+\left[\left(\nabla\times\vec{P}'\right)+\frac{\partial\left(\nabla\cdot\vec{P}'\right)}{\partial t}\right]_{HT} \quad (18)$$

The first part term on the right-hand side means that these terms are not directly influenced by density, which are combined grouped together; the second part term means the direct influence of density variations on storm surges and is accordingly grouped together. The corresponding dynamical equation under the HM model is given as follows:

$$\left(f^2\frac{\partial\eta}{\partial t}+\frac{\partial^3\eta}{\partial t^3}\right)_{HM}=\left\{f\left[\nabla\times\left(\vec{P}+\vec{N}-\vec{\tau}_s+\vec{\tau}_b\right)\right]+\frac{\partial\left[\nabla\cdot\left(\vec{P}+\vec{N}-\vec{\tau}_s+\vec{\tau}_b\right)\right]}{\partial t}\right\}_{HM} \quad (19)$$

We use the HT model as the reference model, as it provides a more accurate representation of the actual conditions due to its higher accuracy. The corresponding terms in the governing equations of the HM and HT models are then subtracted from each other to quantify the storm surge bias and the biases in each dynamical mechanism attributable to density variations, denoted by the subscript MT:

$$\left(f^2\frac{\partial\eta}{\partial t}+\frac{\partial^3\eta}{\partial t^3}\right)_{MT}=\left\{-\left[\left(\nabla\times\vec{P}'\right)+\frac{\partial\left(\nabla\cdot\vec{P}'\right)}{\partial t}\right]\right\}_{MT}+\left\{f\left[\nabla\times\left(\vec{P}+\vec{N}+\vec{\tau}_b\right)\right]+\frac{\partial\left[\nabla\cdot\left(\vec{P}+\vec{N}+\vec{\tau}_b\right)\right]}{\partial t}\right\}_{MT} \quad (20)$$

Since the wind stress is identical in both models, it does not appear in the bias equation. The first term of the dynamical mechanism on the right-hand side of Equation (20) is regarded as the direct influence of density, denoted as Q_{MT_Direct}, where the negative sign has no physical meaning; the second dynamical mechanism term is regarded as the indirect influence of density, denoted as $Q_{MT\_Indirect}$.

https://doi.org/10.5194/egusphere-2026-1581
Preprint. Discussion started: 17 April 2026

The simplified form is as follows:

$$\begin{cases} Q_{MT\_Direct} = \left\{ -\left[\left(\nabla \times \vec{P}' \right) + \dfrac{\partial \left(\nabla \cdot \vec{P}' \right)}{\partial t} \right] \right\}_{MT} \\ Q_{MT\_Indirect} = \left\{ f\left[\nabla \times \left(\vec{P} + \vec{N} + \vec{\tau}_b \right) \right] + \dfrac{\partial \left[\nabla \cdot \left(\vec{P} + \vec{N} + \vec{\tau}_b \right) \right]}{\partial t} \right\}_{MT} \end{cases} \tag{21}$$

Equation (20) is then summarized as follows:

$$\left(f^2 \frac{\partial \eta}{\partial t} \right)_{MT} + \left(\frac{\partial^3 \eta}{\partial t^3} \right)_{MT} = Q_{MT\_Direct} + Q_{MT\_Indirect} \tag{22}$$

Next, we take station S1 as an example to analyze the magnitudes of the individual terms in Equation (22). In Section 3.1, the results indicate that storm surges inside Hangzhou Bay are dominated by low-frequency components, so a low-pass filter is applied to each term in Equation (22). The cutoff frequency of the low-pass filter is determined based on the dominant period at station S1 of 50 h, giving $f_{50} = \frac{1/50}{1/2} = 0.04$,the low-pass filtered results are shown in the figure below. The storm surge difference between HM and HT is predominantly governed by the term $f^2 \frac{\partial \eta}{\partial t}$. Among the dynamical mechanism terms, the one whose temporal variation and magnitude are most consistent with $f^2 \frac{\partial \eta}{\partial t}$ is Q_{MT_Direct} ,showing that the pressure gradient force directly generated by spatial density heterogeneity can produce substantial storm surge variations. It is also evident from the figure that density variations exert an indirect influence on storm surges as well, though the magnitude of this indirect contribution is relatively small and will not be further analyzed.

https://doi.org/10.5194/egusphere-2026-1581
Preprint. Discussion started: 17 April 2026

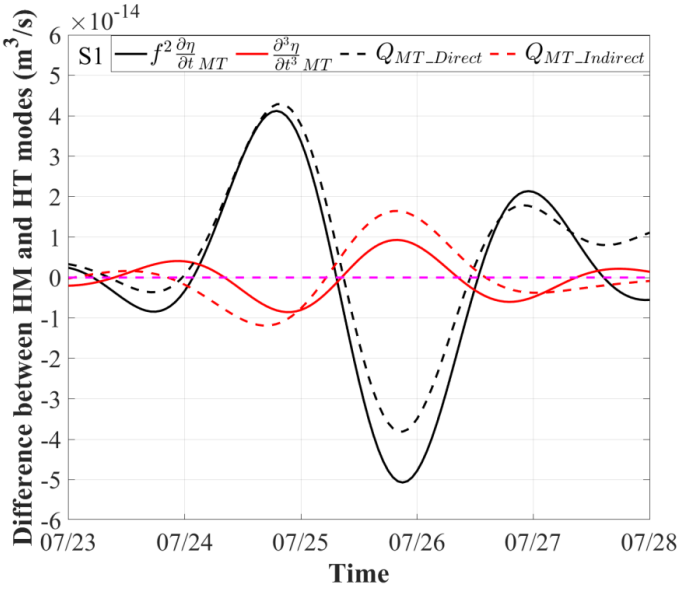

Fig. 8 Differences in storm surges and individual dynamical mechanism terms between HM and HT.

3.5 Diagnostic Equation for Density-Related Storm Surges

Based on the above results, the subsequent analysis in this study will focus on the storm surges generated by Q_{MT_Direct}. The storm surge difference between the two models is primarily attributable to the pressure gradient force $\vec{P}'$,generated by density variations. This mechanism is summarized in Equation (23), and the storm surge variation generated by the divergence and vorticity of $\vec{P}'$ are denoted as $\eta'_{\rho'}$, referred to hereafter as the density-related storm surge.

$$\frac{\partial\eta'_{\rho'}}{\partial t}=\frac{\nabla\times\vec{P}'}{f}+\frac{1}{f^2}\frac{\partial\left(\nabla\cdot\vec{P}'\right)}{\partial t} \tag{23}$$

The difference between the storm surges simulated by HM and HT is denoted as η':

$$\eta'=\eta_{HM}-\eta_{HT} \tag{24}$$

https://doi.org/10.5194/egusphere-2026-1581
Preprint. Discussion started: 17 April 2026

Taking station S1 as an example, the time derivative $\frac{\partial \eta'}{\partial t}$ is compared with the individual terms of Equation (23) to further analyze the underlying causes.

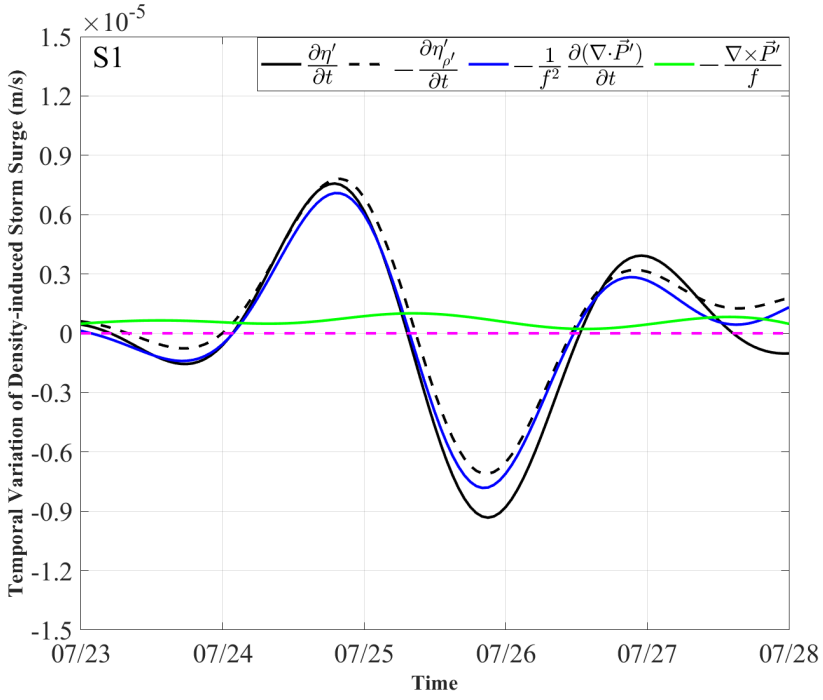

Fig. 9 Comparison of $\frac{\partial \eta'}{\partial t}$ and $\frac{\partial \eta'_{\rho'}}{\partial t}$.

Fig. 9 shows the comparison between $\frac{\partial \eta'}{\partial t}$ and $\frac{\partial \eta'_{\rho'}}{\partial t}$, as well as the individual terms of Equation (23) at station S1, where the negative sign carries no physical meaning. The time variation of the density-related storm surge $\frac{\partial \eta'_{\rho'}}{\partial t}$ is obtained by summing the divergence term $\frac{1}{f^2}\frac{\partial\left(\nabla \cdot \vec{P}'\right)}{\partial t}$ and the vorticity term $\frac{\nabla \times \vec{P}'}{f}$ of the density-related pressure gradient force. As can be seen from the figure, the variations of $\frac{\partial \eta'}{\partial t}$ and $-\frac{\partial \eta'_{\rho'}}{\partial t}$ are broadly consistent, and it can be further inferred that $\frac{\partial \eta'_{\rho'}}{\partial t}$ is primarily driven by $\frac{1}{f^2}\frac{\partial\left(\nabla \cdot \vec{P}'\right)}{\partial t}$,while $\frac{\nabla \times \vec{P}'}{f}$ is negligible.

https://doi.org/10.5194/egusphere-2026-1581
Preprint. Discussion started: 17 April 2026

Given that the mean water depth of the study area is only 10 m, and considering the form of $\vec{P}'$, the vertical variation of density is neglected, yielding the following simplified expression:

$$\begin{aligned}\vec{P}' &= \frac{g}{\rho_0}\left[\int_{-H}^{\eta}\nabla\left(\int_{z}^{\eta}\rho' dz'\right)dz\right]\\ &= \frac{g}{\rho_0}\left\{\int_{-H}^{\eta}\nabla[\rho'(\eta-z)]dz\right\}\\ &= \frac{g}{\rho_0}\left\{\int_{-H}^{\eta}(\eta-z)\nabla\rho' dz\right\}+\frac{g}{\rho_0}\left\{\int_{-H}^{\eta}\rho'\nabla(\eta-z)dz\right\}\\ &= \frac{g\nabla\rho'}{\rho_0}\int_{-H}^{\eta}(\eta-z)dz+\frac{g\rho'}{\rho_0}\int_{-H}^{\eta}\nabla(\eta-z)dz\\ &= \frac{g\left(\frac{1}{2}\eta^2+\eta H+\frac{1}{2}H^2\right)\nabla\rho'}{\rho_0}+\frac{g(\rho'\eta+\rho' H)\nabla\eta}{\rho_0}\end{aligned} \quad (25)$$

Neglecting $\frac{\nabla\times\vec{P}'}{f}$,equation (23) can be rewritten as follows:

$$\begin{aligned}\frac{\partial\eta'_{\rho'}}{\partial t} = \frac{1}{f^2}\frac{\partial\left(\nabla\cdot\vec{P}'\right)}{\partial t} &= \frac{g}{\rho_0 f^2}\frac{\partial}{\partial t}\left\{\nabla\cdot\left[\left(\frac{1}{2}\eta^2+\eta H+\frac{1}{2}H^2\right)\nabla\rho'\right]\right\}+\frac{g}{\rho_0 f^2}\frac{\partial}{\partial t}\{\nabla\cdot[\rho'(\eta+H)\nabla\eta]\}\\ &= \frac{g}{\rho_0 f^2}\frac{\partial}{\partial t}\left[\left(\frac{1}{2}\eta^2+\eta H\right)\Delta\rho'\right]+\frac{g}{\rho_0 f^2}\frac{\partial}{\partial t}\left(\frac{H^2}{2}\Delta\rho'\right)+\frac{g}{\rho_0 f^2}\frac{\partial}{\partial t}\left[\nabla\rho'\cdot\nabla\left(\frac{1}{2}\eta^2+\eta H\right)\right]\\ &\quad+\frac{g}{\rho_0 f^2}\frac{\partial}{\partial t}\left(\nabla\rho'\cdot\frac{\nabla H^2}{2}\right)+\frac{g}{\rho_0 f^2}\frac{\partial}{\partial t}[\rho'(\eta+H)\Delta\eta]+\frac{g}{\rho_0 f^2}\frac{\partial}{\partial t}\{\nabla\eta\cdot[\nabla\rho'(\eta+H)]\}\end{aligned} \quad (26)$$

Since the water depth H is time-independent and the density anomaly ρ' does not vary with time either, the time derivative terms, $\frac{g}{\rho_0 f^2}\frac{\partial}{\partial t}\left(\frac{H^2}{2}\Delta\rho'\right)$and $\frac{g}{\rho_0 f^2}\frac{\partial}{\partial t}\left(\nabla\rho'\cdot\frac{\nabla H^2}{2}\right)$, involving H and ρ' in Equation (21) are both zero. Neglecting these time-invariant terms, the expression for the density-related storm surge $\eta'_{\rho'}$ is given as follows:

$$\begin{aligned}\eta'_{\rho'} = \nabla\cdot\vec{P}' &= \frac{g}{\rho_0 f^2}\left[\left(\frac{1}{2}\eta^2+\eta H\right)\Delta\rho'\right]+\frac{g}{\rho_0 f^2}\left[\nabla\rho'\cdot\nabla\left(\frac{1}{2}\eta^2+\eta H\right)\right]\\ &\quad+\frac{g}{\rho_0 f^2}[\rho'(\eta+H)\Delta\eta]+\frac{g}{\rho_0 f^2}\{\nabla\eta\cdot\nabla[\rho'(\eta+H)]\}\end{aligned} \quad (27)$$

The magnitudes of the individual terms in Equation (22) are calculated based on the model-simulated values as follows:

https://doi.org/10.5194/egusphere-2026-1581
Preprint. Discussion started: 17 April 2026

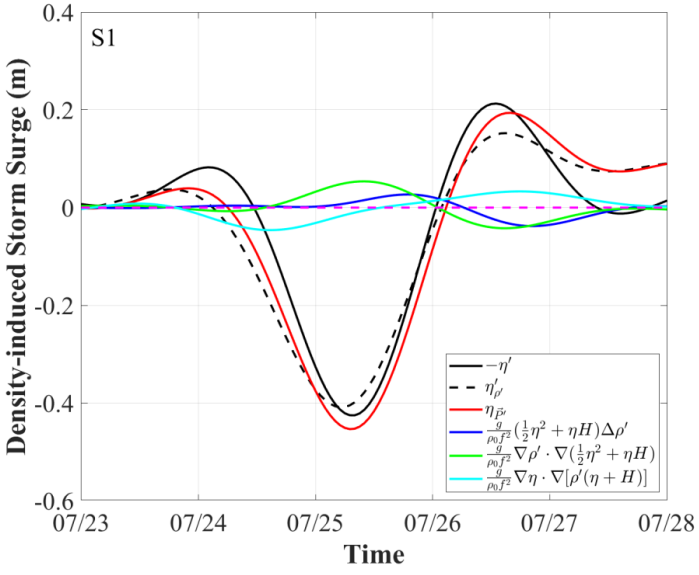

Fig. 10 Comparison of η' and $\eta'_{\rho'}$

As shown in Fig. 8, η' and $-\eta'_{\rho'}$ exhibit broadly consistent temporal variations, with $\frac{g}{\rho_0 f^2}\left[\left(\frac{1}{2}\eta^2+\eta H\right)\Delta\rho'\right]$ playing the dominant role in determining $\eta'_{\rho'}$, namely the coupling term between the storm surge, water depth, and the Laplacian of the density anomaly.

The following analysis examines the overall characteristics of density-related storm surges across the entire study area. Based on the spatial distribution of storm surge periods discussed in Section 3.1, low-frequency storm surges are predominantly distributed within the interior of Hangzhou Bay (120.5°E–121.7°E, 29.9°N–30.8°N). Using the storm surge time series at station S1 as a reference, the moments of maximum surge rise and maximum surge fall are selected for comparison of η' and $\eta'_{\rho'}$ the corresponding spatial distributions.

https://doi.org/10.5194/egusphere-2026-1581
Preprint. Discussion started: 17 April 2026

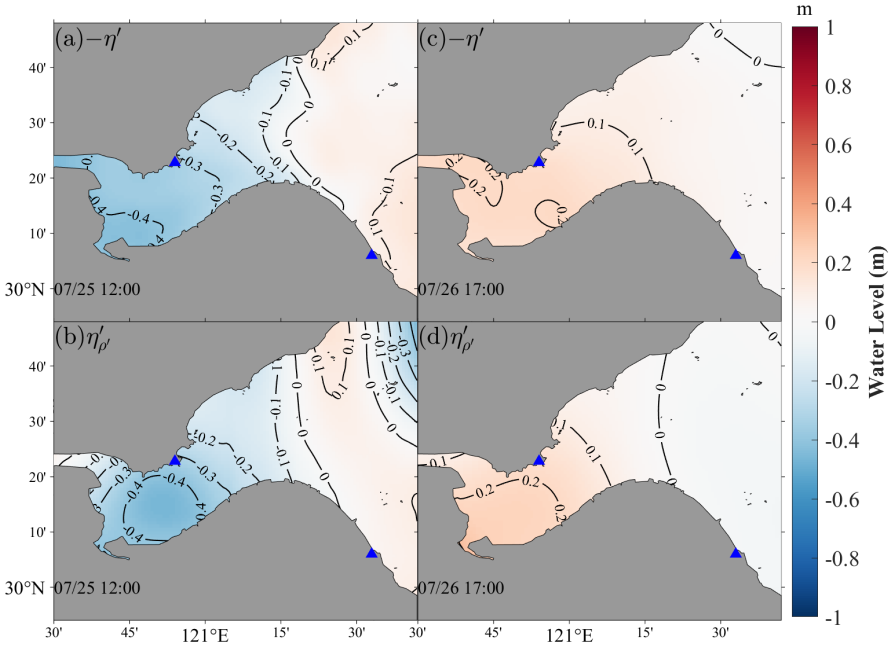

Fig. 11 Spatial distributions at the moments of maximum storm surge rise and maximum storm surge fall.

Fig. 11 shows the spatial distributions of η' and $\eta'_{\rho'}$ at the moments of maximum storm surge rise and maximum storm surge fall. Overall, the values of η' and $\eta'_{\rho'}$ are in close agreement within the interior of Hangzhou Bay at both moments. However, slight discrepancies exist in localized areas: at the moment of maximum surge rise, $\eta'_{\rho'}$ is relatively elevated in the exterior of Hangzhou Bay near the northern bay mouth region, while at the moment of maximum surge fall, $\eta'_{\rho'}$ is relatively elevated in the exterior of Hangzhou Bay near the southern bay mouth region.

Based on the above results, the dominant term in $\eta'_{\rho'}$ is $\frac{g}{\rho_0 f^2}\left[\left(\frac{1}{2}\eta^2+\eta H\right)\Delta\rho'\right]$, in which the primary variable of $\frac{g}{\rho_0 f^2}$ is the Coriolis parameter f .Since the study area is located near 30°N with a relatively small latitudinal extent, the spatial variation of f is neglected, and f is uniformly

https://doi.org/10.5194/egusphere-2026-1581
Preprint. Discussion started: 17 April 2026

computed using the value at 30°N throughout the entire domain. Consequently, $\frac{g}{\rho_0 f^2}$ reduces to a constant, denoted as C_0, with a value of approximately 1.84×10^6. Given that the mean water depth H of the study area is 10 m and the storm surge height is approximately 2–3 m, the contribution of $\frac{1}{2}\eta^2$ is neglected, retaining only ηH, and the storm surge η is replaced by η_{HM} from the homogeneous model for computation. Based on the above analysis, Equation (28) is defined as the diagnostic equation, in which the symbol $\approx$ indicates that the two sides are not strictly equal, but rather that the spatial distribution of $\eta'_{\rho'}$ is approximately inferred from the storm surge–water depth coupling term $C_0\eta H$, the spatial distribution of density ρ, and the Laplacian of the density anomaly $\Delta\rho'$. In this expression, the water depth term H in $C_0\eta H$ is time-invariant, so the temporal variation of this term depends solely on the storm surge η; the Laplacian of the density anomaly $\Delta\rho'$ is the second-order spatial derivative of the density surface, whose spatial variation is inversely related to the undulation trend of the density surface itself. Therefore, the spatiotemporal variation of the density-related storm surge $\eta'_{\rho'}$ can be approximately determined from the spatial distribution of density and the spatiotemporal characteristics of storm surges within the study area. The specific diagnostic procedure is described with reference to Fig. 9 and its caption.

$$\eta'_{\rho'} \approx C_0\eta H\Delta\rho' \tag{28}$$

https://doi.org/10.5194/egusphere-2026-1581
Preprint. Discussion started: 17 April 2026

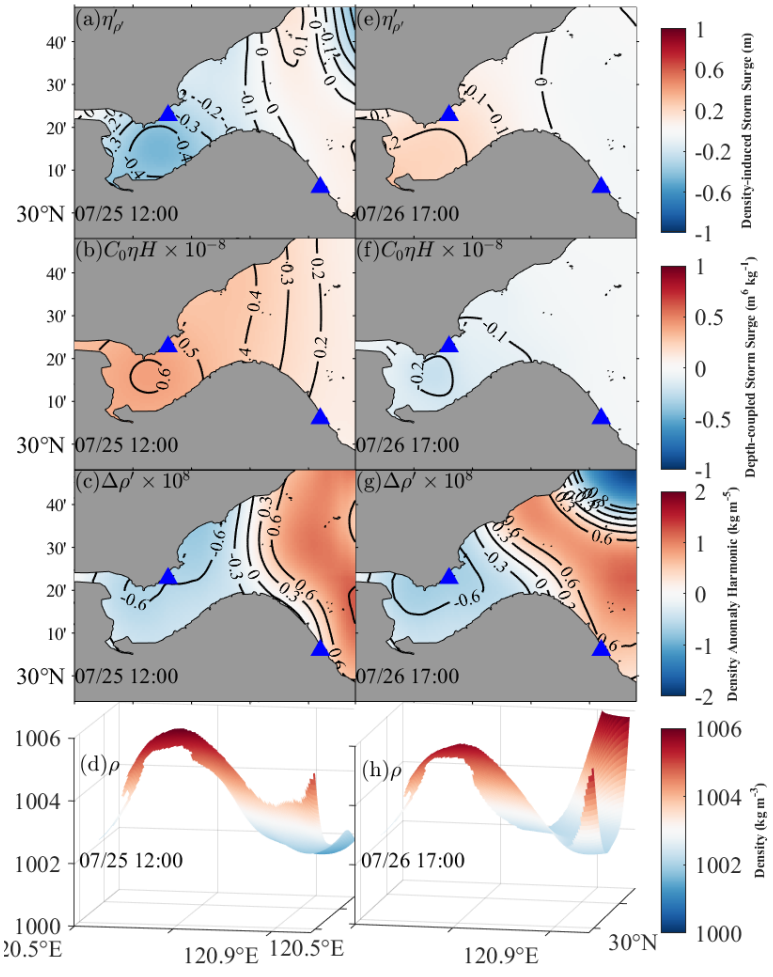

Fig. 12 Spatial distributions of $\eta'_{\rho'}$, $C_0\eta H$, $\Delta\rho'$ and ρ during the periods of storm surge rise and fall.

As indicated by Equation (28), the density-related storm surge results from the coupled effect of density and storm surge. Taking the surge rise period as an example, panels (a)–(d) of Fig. 12 are analyzed. Panel (a) shows the spatial distribution of the density-related storm surge as described in Figure11; during the typhoon surge rising, it is negative inside Hangzhou Bay and positive outside. According to Equation (28), panel (a) is given by multiplying panel (b) and panel (c): panel (b) shows the storm surge rise superimposed on the water depth, with a pronounced water level increase inside

https://doi.org/10.5194/egusphere-2026-1581
Preprint. Discussion started: 17 April 2026

Hangzhou Bay; panel (c) shows the Laplacian of the density anomaly across the entire region, which exhibits a negative interior and positive exterior pattern. Multiplying the two yields, we can get the density-related storm surge shown in panel (a). Further analysis reveals that the spatial distribution of the Laplacian of the density anomaly is fundamentally due to the density distribution in the Hangzhou Bay region, which is characterized by higher density inside and lower density outside the bay. During the surge fall period, panels (e)–(h) similarly satisfy the above distribution pattern. In addition, a large influx of seawater into the exterior of Hangzhou Bay in the later stage results in a high–low–high density distribution across the entire region, though this does not affect the variations inside Hangzhou Bay.

In summary, the diagnostic equation provides a concise and intuitive means of determining the spatial distribution characteristics of density-related storm surges based on the spatial features of storm surges and density variations. This indicates that the differences between the HT and HM models arise not from density variations directly, but from the coupling effect between density and storm surges. This leads to an interesting conclusion.

4 Discussion

4.1 Analysis of the Influence of Spatial density heterogeneity Based on Water Level Type and Timescale

Spatial density heterogeneity influences the simulation accuracy of different water level components (total water levels, astronomical tides, and storm surges) at different timescales to varying degrees. This phenomenon has been observed in both the present study and several previous studies, and will be discussed sequentially below.

In terms of different water level types, spatial density heterogeneity improves more accuracy on storm surge than that of astronomical tide. As shown in Section 3.1, the simulation bias for storm surges in the homogeneous model is far greater than that for astronomical tides. Wang et al. (2021) similarly compared the accuracy improvements for different water levels, including the total water levels, astronomical tides, and residual water levels, the results showed that the improvement in residual water level accuracy far exceeded that of astronomical tides: 94% of the 211 tide gauge stations showed residual water level accuracy improvements of 31%–37%, while 78% of stations

https://doi.org/10.5194/egusphere-2026-1581
Preprint. Discussion started: 17 April 2026

showed astronomical tide accuracy improvements of 13%–18%. Pringle et al. (2019) also compared accuracy improvements for total water levels and residual water levels; they concluded that the total water levels increased from 87% to 93%, while that for the residual water levels increased from 54% to 85%. Although the present study involves a limited number of stations and need more extensive statistical analysis, the combined evidence from these studies consistently indicates that storm surges are more strongly influenced by spatial density heterogeneity.

In terms of different timescales of water levels, spatial density heterogeneity improves the accuracy of long-period water levels to a greater extent than short-period water levels. As shown in Section 3.2, the storm surge periods in this study exceed 50 h, while astronomical tidal periods range from 12 to 24 h, and the degree of accuracy improvement is greater for storm surges than for astronomical tides. Similarly, Wang et al. also found that the degree of accuracy improvement for residual water levels decreases progressively from seasonal, to inter-seasonal, sub-seasonal, and weather timescales. Pringle et al. made a power spectral density analysis of sea level variations recorded at 6-minute intervals, and the results indicated that as frequency increases, the discrepancy between the baroclinic model and observations increases progressively across the semi-annual, monthly/fortnightly, diurnal (K_1, O_1), semi-diurnal (M_2, S_2), and super-tidal periods. Although only two timescales are considered in the present study, limiting the number of comparative stages, the combined evidence from these two studies consistently indicates that spatial density heterogeneity exerts a more pronounced influence on low-frequency water level variations.

4.2 Discussion on the Mechanisms by Which Spatial density heterogeneity Influences Storm Surges

In examining the influence of spatial density heterogeneity on storm surges on storm surges, many previous studies have approached the problem primarily from the perspective of phenomenological characteristics, whereas the present study focuses on the dynamical mechanisms of seawater. Compared to the former approach, the methodology and findings of this study are more rigorous and well-founded, while also offering novelty. Not only does this study provide a detailed

https://doi.org/10.5194/egusphere-2026-1581
Preprint. Discussion started: 17 April 2026

and comprehensive explanation of how spatial density heterogeneity influences storm surges, but it also derives a diagnostic relationship between density and storm surges, which is of significant importance for deepening the understanding of storm surge dynamics and related ocean dynamical processes.

Spatial density heterogeneity reflects the spatial variability of seawater density, which tends to give rise to distinctive water mass structures and environmental backgrounds, such as vertical density stratification, horizontal circulation, and fronts. Many studies have summarized and analogized these phenomenological characteristics to briefly identify the mechanisms by which Spatial density heterogeneity influences storm surges, broadly categorizing them into three types: coastal trapped waves, bottom friction, and horizontal pressure gradient force. The present study also identifies the influence of the horizontal pressure gradient force from the perspective of ocean dynamical mechanisms, though the specific mechanism differs from those identified in prior studies. Overall, spatial density heterogeneity can influence storm surges through multiple pathways, and each case warrants individual discussion.

The regions where coastal trapped waves occur frequently precisely those where storm surge forecast accuracy improves. This phenomenon has been observed in both Kodaira et al. (2016) and Wang et al.(2022), however, the specific mechanisms require further analysis. Regions where coastal trapped waves commonly occur tend to exhibit pronounced stratification, and there are two possible pathways existing through which density stratification influence storm surge forecast accuracy: density stratification may affect storm surge forecast accuracy indirectly by exciting coastal trapped waves, or it may exert a direct influence independently. If the reason were the former, future research should focus on analyzing the relationship between coastal trapped waves and storm surges, which also involves the coupling processes and mechanisms between water levels at different spatiotemporal scales. If the latter , future research should focus on the relationship between the density stratification and the storm surge. Based on the content of Kodaira et al. (2016) and Wang et al.(2022), coastal trapped waves typically have spatial scales of hundreds to thousands of kilometers, with temporal scales of variation reaching up to several months. In contrast, storm surges, which are of widespread concern, typically occur in nearshore regions and are strongly influenced by typhoon

https://doi.org/10.5194/egusphere-2026-1581
Preprint. Discussion started: 17 April 2026

tracks, the water levels change dramatically over short time periods and small spatial extents, with maximum spatial scales of only a few hundred kilometers. The generation mechanisms of these two types of water level variations are inherently different. Therefore, the role of spatial density heterogeneity in influencing water level accuracy may operate either through coastal trapped waves or through other processes, and the specific mechanisms remain to be clarified.

The mechanisms by which bottom friction influences storm surges are also unclear. Both Orton et al. (2012) and Kodaira et al.(2016) have observed that density stratification affects storm surge forecast accuracy. Orton et al. thought that the changes in storm surge forecast accuracy are simply due to the effects of bottom friction ,which has been found in Muller's work on the transport mechanisms and amplitude variations of tides under density stratification. However, the evolution of storm surges differs from that of tides, and the specific mechanisms warrant separate discussion. Muller's study investigated the influence of density stratification on tidal transport and amplitude using a combination of dynamical equations and numerical modeling. He concluded that the eddy viscosity coefficient, pycnocline depth, and bottom friction exert a combined influence. To focus specifically on the effect of bottom friction, he neglected the advection, he cared more about the influence of the Coriolis force; in the Northern Hemisphere, only the clockwise tidal current component has its transport magnitude altered by density stratification. Under stratified conditions, the eddy viscosity coefficient above the pycnocline is relatively low and current velocities are relatively large, reaching a peak at the pycnocline itself, while strong shear develops below the pycnocline and current velocities decay more rapidly. When water depth is large, the velocity attenuation below the pycnocline dominates, resulting in overall transport that is smaller than under well-mixed conditions; when water depth is small, the larger velocities above the pycnocline dominate, resulting in overall transport that exceeds that under well-mixed conditions. Since the pycnocline depth varies seasonally, tidal transport and amplitude also vary accordingly. It is worth noting that Muller's study also addresses the influence of surface wind stress on the eddy viscosity coefficient, finding that increasing surface wind speed leads to an increase in the eddy viscosity coefficient above the pycnocline and corresponding changes in current velocity. However, the

https://doi.org/10.5194/egusphere-2026-1581
Preprint. Discussion started: 17 April 2026

maximum wind stress considered in that study was only 4.5 m/s, which did not significantly affect the results, which means that the pycnocline depth is affected almost by the bottom friction. In storm surge research, wind stress is a critical factor and wind speeds are generally far in excess of 4.5 m/s; therefore, whether the conclusions drawn above remain valid when wind stress effects are the primary consideration requires further verification.

In this study, we draw a conclusion that the influence of the pressure gradient force generated by spatial density heterogeneity affect the storm surge forecast accuracy. While Ye et al.(2020) and Pringle et al.(2019) also noted the influence of the pressure gradient force, but the processes and mechanisms involved differ, leading to differences in the duration and magnitude of storm surge water level variations; the specific role of density variations therefore warrants careful distinction. In the present study, a key finding is that throughout the pre-, during-, and post-typhoon stages, the density field does not change in regions where storm surge forecast accuracy varies considerably, instead, it acts as a background field that couples with the storm surge to alter its accuracy. The duration of this influence is consistent with that of the storm surge itself, and its magnitude is jointly determined by spatial density heterogeneity and the storm surge. In contrast, Ye et al. and Pringle et al. focused on changes in the density field itself occurring during typhoon passage and their subsequent influence on storm surge forecast accuracy. Both studies strengthened the influence of the cold wake left by the typhoon, and Ye et al. thought of the influence of the large-scale Gulf Stream, the density variations of which continued to affect water levels for approximately 30 days after the storm. Pringle et al. similarly noted that density variations continued to influence water levels for approximately 15 days following the storm surge. However, the magnitude and the lasting time of water level changes induced by density variations still requires precise quantification. Overall, although the pressure gradient force is a relatively intuitive factor, the specific mechanisms must be determined in conjunction with the spatial distribution of density and the dynamical behavior of storm surges.

5 Conclusions

https://doi.org/10.5194/egusphere-2026-1581
Preprint. Discussion started: 17 April 2026

This study designed a homogeneous ocean model and a heterogeneous ocean model to investigate the influence of spatial density heterogeneity on storm surge characteristics in Hangzhou Bay and its adjacent waters during Typhoon In-Fa. Under the heterogeneous ocean model, the simulation accuracy of different water level types, including astronomical tides and storm surges, was improved, with a greater degree of improvement for storm surges. Furthermore, the influence of spatial density heterogeneity on water levels at different timescales also exhibits a systematic pattern, with a greater degree of accuracy improvement for long-period water levels (e.g., storm surges with periods exceeding 50 h) than for short-period water levels (e.g., astronomical tides with periods of 12–24 h).

This study analyzed the reasons for the improved storm surge forecast accuracy under the heterogeneous ocean model from the perspective of seawater dynamics. The governing equation for storm surge motion was derived, and by integrating the period characteristics with spectral analysis of storm surges, the mechanisms by which spatial density heterogeneity influences storm surges with frequencies below the inertial frequency were primarily discussed. The pressure gradient force generated by spatial density heterogeneity was identified as the principal cause of the accuracy improvement. Furthermore, a diagnostic relationship between density and storm surges was established, whereby spatial density heterogeneity acts as a background field that couples with storm surges to alter their accuracy.

This study also has several limitations. Regarding the variation characteristics of storm surges and other water levels under the heterogeneous ocean model, future work should incorporate additional typhoon cases and tide gauge records for statistical analysis in order to derive more representative conclusions. Regarding the reasons for the improved storm surge forecast accuracy under the heterogeneous ocean model, the high-frequency components remain unexplained, and the individual dynamical processes in the diagnostic analysis require precise quantification for magnitude for comparison; such quantification would render the findings more rigorous.

In summary, spatial density heterogeneity plays a significant role in improving water level forecast accuracy and advancing research on related scientific questions. Its influence is multifaceted and cannot be neglected, and the underlying mechanisms are diverse and require case-specific analysis, including but not limited to coastal trapped waves, bottom friction, and pressure gradient

https://doi.org/10.5194/egusphere-2026-1581
Preprint. Discussion started: 17 April 2026

force. Incorporating this factor in future numerical simulations would not only improve forecast accuracy and enhance the practical value of forecasting, but also provide important insights for research into related scientific problems, such as storm surge simulation, sea level prediction, cross-scale current transport, and cross-scale energy cascades in water level variations.

Acknowledgements: The authors gratefully acknowledge the data providers and platforms that made this study possible. These include the Oregon State University Tidal Prediction Software (OTPS; http://volkov.oce.orst.edu/tides) for tidal constituent data, the Hybrid Coordinate Ocean Model (HYCOM; https://www.hycom.org/) for temperature and salinity data, the Yangtze River Hydrology Network (www.cjh.com.cn) and the Ministry of Water Resources (http://www.mwr.gov.cn/sj/tjgb/zghlnsgb/) for river discharge data, the OAFlux project of the National Center for Atmospheric Research (https://climatedataguide.ucar.edu/climate-data/oaflux) for air–sea flux data, and the China Typhoon Meteorological Network (http://typhoon.nmc.cn) for track and intensity data of Typhoon In-Fa

This work was supported by the Key Research and Development Program of the Ministry of Science and Technology of China (Grant No. 2023YFC3008100), the Sino-German Marine Science and Technology Cooperation Framework Project (Grant No. WTZ03V01762-NECO), and the UN Ocean Decade Project (CSK-2/08/2023-KEES).

Special Note: The original manuscript of this paper was written independently by me in Chinese; I utilized AI tools to generate portions of the translation.

https://doi.org/10.5194/egusphere-2026-1581
Preprint. Discussion started: 17 April 2026

References

Hou, J., Yu, F., Yuan, Y., & Fu, X. (2011). Spatiotemporal distribution of major typhoon storm surges affecting China. Marine Science Bulletin, 30(5), 535–539.

Yu, F., et al. (2020). Modern Storm Surge Forecasting Technology and Applications. Beijing: Science Press.

Ministry of Natural Resources. (2024). 2023 China Marine Disaster Bulletin. [Online document]. Available at: http://101.231.140.106/gk/gbytj/202405/t20240510_28037.shtml [Accessed: October 10, 2024].

Bernier, N. B., & Thompson, K. R.(2015). Deterministic and ensemble storm surge prediction for Atlantic Canada with lead times of hours to ten days. Ocean modelling (Oxford),86(114-127. DOI: 10.1016/j.ocemod.2014.12.002.

Chen, C. S., Liu, H. D., & Beardsley, R. C.(2003). An unstructured grid, finite-volume, three-dimensional, primitive equations ocean model: Application to coastal ocean and estuaries. Journal of Atmospheric and Oceanic Technology,20(1), 159-186. DOI: 10.1175/1520-0426(2003)020<0159:AUGFVT>2.0.CO;2.

Clarke, A. J., & Shi, C.(1991). Critical frequencies at ocean boundaries. Journal of Geophysical Research: Oceans,96(C6), 10731-10738.

Doodson, A. T.(1956). Tides and storm surges in a long uniform gulf. Proceedings of the Royal Society of London. Series A, Mathematical and physical sciences,237(1210), 325-343. DOI: 10.1098/rspa.1956.0180.

Heaps, N. S.(1969). A Two-Dimensional Numerical Sea Model. Philosophical transactions of the Royal Society of London. Series A: Mathematical and physical sciences,265(1160), 93-137. DOI: 10.1098/rsta.1969.0041.

Hetzel, Y., Janekovic, I., & Pattiaratchi, C.(2017). Assessing the ability of storm surge models to simulate coastal trapped waves around Australia. 586-592): Engineers Australia, PIANC Australia and Institute of Professional Engineers.

Kodaira, T., Thompson, K. R., & Bernier, N. B.(2016). The effect of density stratification on the prediction of global storm surges. Ocean Dynamics,66(1733-1743.

Orton, P., Georgas, N., Blumberg, A., & Pullen, J.(2012). Detailed modeling of recent severe storm tides in estuaries of the New York City region. Journal of Geophysical Research: Oceans,117(C9).

Pringle, W. J., Gonzalez Lopez, J., Joyce, B. R., Westerink, J. J., & van der Westhuysen, A. J.(2019). Baroclinic coupling improves depth-integrated modeling of coastal sea level variations around Puerto Rico and the US Virgin Islands. Journal of Geophysical Research: Oceans,124(3), 2196-

https://doi.org/10.5194/egusphere-2026-1581
Preprint. Discussion started: 17 April 2026

2217.

Wang, P., Bernier, N. B., & Thompson, K. R.(2022). Adding baroclinicity to a global operational model for forecasting total water level: Approach and impact. Ocean Modelling,174(102031.

Xuan, J., Ding, R., & Zhou, F.(2021). Storm surge risk under various strengths and translation speeds of landfalling tropical cyclones. Environmental Research Letters,16(12), 124055.